ACADEMIC PRESS

Available online at www.sciencedirect.com

SCIENCE DIRECT®

Journal of Sound and Vibration 260 (2003) 453–476

JOURNAL OF SOUND AND VIBRATION

www.elsevier.com/locate/jsvi

Active damping of a micro-cantilever piezo-composite beam

M. Collet*, V. Walter, P. Delobelle

Laboratoire de Mécanique Appliquée R. Chaléat UMR-CNRS 6604, 24 chemin de l'Epitaphe, 25000 Besançon, France

Received 29 June 2001; accepted 18 March 2002

Abstract

Thick PZT films are of major interest in the actuation of mechanical structures. One of the promising fields deals with active damping. Since it is a dynamic application, hard-PZT type of screen-printed films are suited to this kind of use. Nevertheless, the drop in dielectric, ferroelectric and piezoelectric properties induced by the fabrication process is a serious constraint and it needs to be evaluated. The first section of this paper will present the mechanical system used for the experimental investigations. These investigations look to quantify the electromechanical properties of the films once the deposition process is achieved. The experimental observations highlighting the efficiency of hard-PZT thick films in active damping despite the drop in the electromechanical properties will then be considered. The control strategy used in the experiments can be called pseudo-direct-velocity feedback. Then the constitutive relations of the composites will be needed to derive the roots locus analysis by means of finite element modelling on one hand and through the roots of the partial derivative equations on the other hand. The unconditional stability of the uncollocated system will be demonstrated and its typical asymptotic behavior when the gain tends towards infinity will be explained.

1. Introduction

Piezoelectric actuators have proved to be effective control devices for active control of structural vibrations and are now used in a wide range of engineering applications. Piezo materials can be integrated in various structural components such as distributed sensors and active dampers of vibrations. Preumont [1] and Banks and Smith [2] present a large overview of these material applications.

One of the most widely used piezo materials in active control are piezoceramics such as PZT because of their large bandwidth, their mechanical simplicity and their mechanical power to

*Corresponding author.
E-mail address: manuel.collet@univ.fcomte.fr (M. Collet).

0022-460X/03/$ - see front matter
PII: S0022-460X(02)00948-3

produce controlling forces. Furthermore, many works dealing with the modelling of the piezoelectric material can be found in the literature. The induced electromechanical coupling and the partial derivative equations modelling the direct and the reverse effects generated by a distributed piezoelectric layer have been studied in Refs. [2–7].

The main problem in using piezoelectric transducers to control a large structure is to guarantee efficiency. Indeed, the material produces a controlling stress which is much smaller than the natural mechanical one. Thus, whatever the feedback control strategy is, the experimental tests lead to active damping without any modification of the conservative behavior of the structure investigated. The damping ratio can reach about 20% on the first modes of the structure. Nevertheless, this value is interesting for many engineering applications [1,8,9]. Similar remarks can be made concerning the application of feedforward strategies, as can be observed in [10,11]. Preumont [1] describes the properties of each approach with an emphasis on the advantages and the disadvantages of many strategies. All these studies lead to the conclusion that the only stable, robust and efficient class of feedback strategy to be implemented in a mechanical structure is the collocated active damping feedback strategy. Even if some studies considered optimizing uncollocated transducers, such as, for example Refs. [5,12,13] and if it is known that the boundary uncollocated approach is much more efficient (see Refs. [14,15]), it seems difficult today to use the uncollocated strategy in industrial applications.

In this context, the MicroElectroMechanical Systems one seems to be of interest in improving the mechanical efficiency of structural active control. These systems can be distributed over a structure and are very powerful since they induce a very high level of stress density. They can effectively present a good opportunity for a large class of problems such as waves control [16] and control of the mechanical interaction or the stabilization of a microsystem such as those described in Ref. [17]. In the initial investigations on the use of a microcontrolling system, the control of a micro-beam totally covered by a piezoelectric, PZT, film is studied. This sample system can be considered as a suspension element able to support very light and sensitive systems such as a frequency generator. In this system, it is possible to cover the entire structure with piezoelectric material, which is not possible on large structures. The mechanical properties of this micro-controlling system are also studied in terms of mechanical characterization of the hard-PZT screen-printed films as in [18] and of theoretical/experimental analysis of the properties of this high power control strategy.

Since this study is a dynamic application, hard-PZT screen-printed films are suited to this kind of use avoiding the classical problem of delamination in the macroscopic application [19]. Nevertheless, the drop in dielectric, ferroelectric and piezoelectric properties induced by the fabrication process is a serious constraint and it needs to be evaluated. The first section of this paper will present and model the mechanical system used for the experimental investigations. These investigations look to quantify the electromechanical properties of the films once the deposition process is achieved. Then the experimental observations highlighting the efficiency of hard-PZT thick films in active damping despite the drop in the electromechanical properties will be described. The control strategy used in the experiments can be called pseudo-direct-velocity feedback. In order to analyze this control, the roots locus analysis will be derived by means of finite element modelling on one hand and through the roots of the partial derivative equations on the other hand. Some numerical errors which can occur in computing the root locus by finite element approach will be pointed out and the unconditional stability of the system correlated with the experimental observations will be proved.

2. Theoretical modelling

The mechanical system studied is shown in Fig. 1. It deals with an alumina cantilever beam on which a PZT film is screen-printed [13]. The constitutive layers of the cantilever beams are also shown in Fig. 1.

2.1. Constitutive relations of the laminated piezocomposite

The piezoelectric layer is assumed to be polarized along (Oz) and all materials are assumed to be isotropic or isotropic in the plane (Oxz). Consider the bending motion in plane (Oxz) of an Euler–Bernoulli beam (see Fig. 2), the piezoelectric state equation can be restricted in the following equations [2,5]:

$$\sigma_{xx}(x,z,t) = E_p \varepsilon_{xx}(x,z,t) - e_{31}E \quad \forall (x,z) \in \Omega_p,$$
$$D_z = e_{31}\varepsilon_{xx}(x,z,t) + \epsilon E \quad \forall (x,z) \in \Omega_p, \tag{1}$$

where σ_{xx} is the xx component of the stress tensor, ε_{xx} is the corresponding strain, the Young's modulus of the piezoelectric layer E_p is assumed to be independent of the thickness, e_{31} is the piezoelectric constant, E is the electric field, D_z the electric displacement along the polarization axis (Oz) and ϵ is the dielectric permittivity. The first equation reflects the reverse piezoelectric coupling effect and the second one expresses the direct one. The electric potential V as defined in Eq. (2) is introduced by assuming the linear variation of E along the thickness negligible in comparison with the constant part [2,5]. Theoretically speaking, the potential V should be quadratic with respect to z:

$$V = -Eh_p. \tag{2}$$

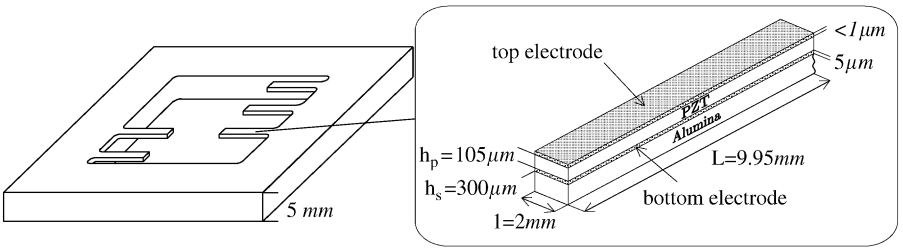

Fig. 1. Geometry of the mechanical system.

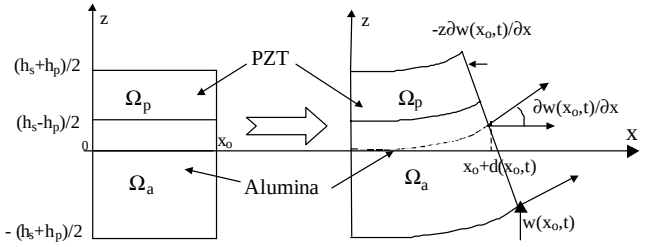

Fig. 2. Kinematical assumptions of Kirchoff–Love homogenization technique.

Similarly, the constitutive relation for the alumina layer is given by the following equation:

$$\sigma_{xx}(x,z,t) = E_s \varepsilon_{xx}(x,z,t) \quad \forall (x,z) \in \Omega_s. \tag{3}$$

The bending displacement of the cross-section of the considered Euler–Bernoulli beam is described in Fig. 2. The corresponding displacement $d(x,z)$ is thus given by the equation,

$$d(x,z,t) = d(x,t) - z\frac{\partial w(x,t)}{\partial x}, \tag{4}$$

where $d(x,t)$ is the displacement along Ox at $z=0$, and $w(x,t)$ is the transverse displacement of the section along Oz. The location of the plane Oxy in the thickness does not matter as far as the computation is done according to this choice. Here, $z=0$ is chosen to be in the middle of the composite as shown in Fig. 2 and for any other choice the same computation must be done. The corresponding strain ε_{xx} is then given in the equation

$$\varepsilon_{xx}(x,z,t) = \frac{\partial d(x,t)}{\partial x} - z\frac{\partial^2 w(x,t)}{\partial x^2}. \tag{5}$$

All these assumptions lead to a Kirchoff–Love homogenization of the motions in the lamina. The expressions of the in-plane normal force and the bending moment along Oy applied on each cross-section are given by the equations,

$$N(x,t) = \int_{-(h_s+h_p)/2}^{(h_s+h_p)/2} \sigma_{xx}(x,z,t) l \, \mathrm{d}z,$$

$$M(x,t) = \int_{-(h_s+h_p)/2}^{(h_s+h_p)/2} \sigma_{xx}(x,z,t) z l \, \mathrm{d}z. \tag{6}$$

Introducing Eqs. (3), (1) and (5) into Eq. (6) leads to the classical constitutive relations of the composites relating the in-plane force $N(x,t)$ and the bending moment $M(x,t)$ to the normal, transverse displacements $d(x,t)$, $w(x,t)$ and the input voltage $V(t)$:

$$N(x,t) = A_{11}\frac{\partial d(x,t)}{\partial x} + B_{11}\left(-\frac{\partial^2 w(x,t)}{\partial x^2}\right) + l e_{31} V(t),$$

$$M(x,t) = B_{11}\frac{\partial d(x,t)}{\partial x} + D_{11}\left(-\frac{\partial^2 w(x,t)}{\partial x^2}\right) + \frac{h_s}{2} l e_{31} V(t), \tag{7}$$

where the homogenized stiffness coefficients are given by

$$A_{11} = (E_s h_s + E_p h_p) l,$$

$$B_{11} = \frac{E_p - E_s}{2} h_p h_s l,$$

$$D_{11} = \frac{E_s h_s (h_s^2 + 3h_p^2) + E_p h_p (h_p^2 + 3h_s^2)}{12} l. \tag{8}$$

Eqs. (7) show that the in-plane and bending motions are coupled through the term B_{11}. It can also be seen that a control term proportional to the applied voltage V and induced by the reverse piezoelectric effect appears in each constitutive equation of (7).

The dynamical equilibrium of the composite Euler–Bernoulli beam described in Fig. 1 is defined in the following equations:

$$\begin{aligned}
&\bar{\rho}\frac{\partial^2 d(x,t)}{\partial t^2} - R\frac{\partial^3 w(x,t)}{\partial t^2 \partial x} - \frac{\partial N(x,t)}{\partial x} = 0 \quad \forall x \in]0, L[,\\
&\bar{\rho}\frac{\partial^2 w(x,t)}{\partial t^2} + R\frac{\partial^3 d(x,t)}{\partial t^2 \partial x} - I\frac{\partial^4 w(x,t)}{\partial^2 t \partial^2 x} - \frac{\partial^2 M(x,t)}{\partial x^2} = 0 \quad \forall x \in]0, L[,\\
&\quad + \text{initial conditions},
\end{aligned} \tag{9}$$

where $\bar{\rho}$, R and $I = \int_{-h/2}^{h/2}(1, z, z^2)\rho(z)\,\mathrm{d}z$ are, respectively, the mass density of the materials, the coupling kinematic term and the quadratic inertia. These two last terms (R and I) are neglected in the classic Euler–Bernoulli approach and are thus not considered. The corresponding boundary conditions are given by the equations,

$$\begin{aligned}
&w(0,t) = d(0,t) = \frac{\partial w(0,t)}{\partial x} = 0,\\
&N(L,t) = M(L,t) = T(L,t) = 0,
\end{aligned} \tag{10}$$

where T is the shear force ($T = -\partial M/\partial x$).

Since the piezoelectric layer completely covers the beam, the integration of Eq. (7) in Eqs. (9) and (10) gives the global equations of the system expressed in the equations,

$$\begin{aligned}
&\bar{\rho}\frac{\partial^2 d(x,t)}{\partial t^2} - A_{11}\frac{\partial^2 d(x,t)}{\partial x^2} + B_{11}\frac{\partial^3 w(x,t)}{\partial x^3} = 0 \quad \forall x \in]0, L[,\\
&\bar{\rho}\frac{\partial^2 w(x,t)}{\partial t^2} - B_{11}\frac{\partial^3 d(x,t)}{\partial x^3} + D_{11}\frac{\partial^4 w(x,t)}{\partial x^4} = 0 \quad \forall x \in]0, L[,\\
&\quad + \text{initial conditions}.
\end{aligned} \tag{11}$$

The boundary conditions are given in the equations,

$$\begin{aligned}
&w(0,t) = d(0,t) = \frac{\partial w(0,t)}{\partial x} = 0,\\
&A_{11}\frac{\partial d(L,t)}{\partial x} - B_{11}\frac{\partial^2 w(L,t)}{\partial x^2} = -le_{31}V(t),\\
&-B_{11}\frac{\partial d(L,t)}{\partial x} + D_{11}\frac{\partial^2 w(L,t)}{\partial x^2} = \frac{h_s}{2}le_{31}V(t),\\
&-B_{11}\frac{\partial^2 d(L,t)}{\partial x^2} + D_{11}\frac{\partial^3 w(L,t)}{\partial x^3} = 0.
\end{aligned} \tag{12}$$

In the following developments, the kinetic energy associated to the term $\bar{\rho}\partial^2 d(x,t)/\partial t^2$ in the in-plane motion equation (11) is assumed to be negligible. By considering the static response of the in-plane motion, the corresponding constitutive equation (the first equation in (11)) can be

simplified as in

$$\frac{\partial^2 d(x,t)}{\partial x^2} = \frac{B_{11}}{A_{11}} \frac{\partial^3 w(x,t)}{\partial x^3} \quad \forall x \in]0, L[. \tag{13}$$

The first equation (11) is thus condensed in the sense of Guyan. The new system of equations governing the motion of the system is also written as

$$\bar{\rho} \frac{\partial^2 w(x,t)}{\partial t^2} + E_{co} I_{co} \frac{\partial^4 w(x,t)}{\partial x^4} = 0 \quad \forall x \in]0, L[,$$
$$+ \text{ initial conditions}, \tag{14}$$

where $E_{co} I_{co} = (D_{11} - B_{11}^2/A_{11})$. The associated boundary equations are given in the following equations:

$$w(0,t) = \frac{\partial w(0,t)}{\partial x} = 0,$$
$$E_{co} I_{co} \frac{\partial^2 w(L,t)}{\partial x^2} = G_p V(t),$$
$$\frac{\partial^3 w(L,t)}{\partial x^3} = 0, \tag{15}$$

where $G_p = (h_s/2 - B_{11}/A_{11}) l e_{31}$ and $e_{31} = d_{31} E_p$.

Thus, the classical set of equations for a bent beam with a modified stiffness are obtained. The force induced by the voltage is the pure bending torque applied at the boundary limit of the piezoceramic layer ($x = L$). These results correspond to those reported by other authors [2,5,12].

3. Experimental investigations

3.1. Fabrication of the samples

The mechanical system (Fig. 1) is a rack of alumina cantilever beams on which a PZT film is screen-printed [18]. The alumina beams are thus clamped at one end to a stiff frame so that good clamping conditions are guaranteed. The constitutive layers of the cantilever beams are also shown in Fig. 1. The first layer is an Ag–Pd bottom electrode screen printed on the alumina substrate. The second layer consists of the active material, the hard-PZT material. This active layer is also screen printed using a paste containing a powder of $PbSr(Zr_{0.455}Ti_{0.455}W_{0.036}Sn_{0.036}Mn_{0.028})$, fabricated by the Ferroelectricity and Electrical Engineering Laboratory (Lyon, France) [20]. The top layer is a sputtered gold electrode. Once the fabrication process is finished, it is necessary to pole the film so that it will exhibit better dielectric, ferroelectric and piezoelectric properties. It is known that the deposition process always induces a loss of properties compared to the bulk material. As a consequence, it is worth making an electromechanical characterization to determine the elastic modulus E_p and the piezoelectric coefficient d_{31} (or $e_{31} = E_p d_{31}$) of the film since it will be needed in the later theoretical development of this paper.

3.2. Electromechanical characterization

3.2.1. Mechanical tests

The mechanical experiments involve a dynamic bending test, a quasi-static bending test and a nanoindentation test. Both bending tests end up with an experimental parameter X that will allow the computation of the elastic modulus. The Young's modulus is indeed the positive solution of the second order polynomial given by

$$AE_p^2 + BE_p + C = 0 \tag{16}$$

with

$$A = h_p^4,$$

$$B = 2E_s h_s h_p (2h_s^2 + 2h_p^2 + 3h_s h_p) - h_p X,$$

$$C = E_s^2 h_s^4 - E_s h_s X, \tag{17}$$

where the parameters E_i and h_i are, respectively, the elastic modulus and the thickness. The subscripts $i = s$ and p refer to the substrate and the piezoelectric film. For the dynamic test

$$X_{dyn} = \frac{48\pi^2 L^4 (h_p \rho_p + h_s \rho_s)}{p_i^4} (f_i)_{exp}^2, \tag{18}$$

where L is the length of the beam, ρ_p and ρ_s are, respectively, the mass density of the piezoelectric film and the substrate, f_i and p_i are, respectively, the experimental eigenfrequency and the frequency parameter of the ith mode. Note that the porosity of the piezoelectric film is taken into account in the value of ρ_p.

For the quasi-static test, the value of X is

$$X_{sta} = \frac{4L^3}{l} \left(\frac{F}{\delta} \right)_{exp}, \tag{19}$$

where F is the applied load, δ the corresponding deflection and l is the width of the beam.

In the case of the nanoindentation test, the value of the elastic modulus is expressed in

$$\frac{E}{(1 - \nu^2)} = \left(\frac{2\sqrt{A}}{\sqrt{\pi}} \left(\frac{\mathrm{d}h}{\mathrm{d}P} \right)_{exp} - \frac{1 - \nu_i^2}{E_i} \right)^{-1}, \tag{20}$$

where ν is the Poisson's ratio of the tested material (assuming to be equal to 0.3), A is the projected contact area, $(\mathrm{d}P/\mathrm{d}h)_{exp}$ is the experimental contact stiffness and E_i and ν_i are, respectively, the Young's modulus and Poisson's ratio for diamond [21].

Table 1 summarizes the results derived from the different tests. In this table, $N_{measure}$ represents the number of measures performed for both types of materials, the substrate and the piezoelectric film. It can be seen that the results are homogeneous from one test to another. In the case of alumina, the difference between the calculated value and the value of the bulk is roughly around 10 GPa, which is less than 3% of the bulk. For the hard-PZT, the values calculated from the different tests are much lower than the value of the bulk material. It is thought to be related to the

Table 1
Elastic modulus of alumina and hard-PZT calculated from the different mechanical tests

	Al_2O_3	Hard-PZT
$N_{measure}$	15	22
$E_{dynamic}$ (GPa)	335 ± 5	19 ± 6
$N_{measure}$	71	19
E_{static} (GPa)	340 ± 8	21 ± 8
$N_{measure}$	20	30
E_{nano} (GPa)	341 ± 45	29 ± 4
E_{bulk} (GPa)	350	94

Table 1

porosity of the film. In this case, the porosity represents indeed near 50% of the total volume of the film, which causes a serious drop in elastic properties.

3.2.2. Electromechanical tests

Once the mechanical properties of the films are determined, the influence of the deposition process on the piezoelectric coefficient d_{31} can be studied. This coefficient relates the strain in the x direction when the film is subjected to a voltage in the perpendicular z direction. For a piezocomposite cantilever beam, one can derive the expression of d_{31}:

$$d_{31} = -\frac{4E_{co}I_{co}(E_s h_s + E_p h_p)}{E_s E_p h_s (h_s + h_f) l L^2} \frac{\delta}{V}, \tag{21}$$

where V is the applied voltage, δ is the corresponding displacement at the free end of the beam and

$$E_{co}I_{co} = \left(\frac{E_s^2 h_s^4 + 2E_s E_p h_s h_p (2h_p^2 + 3h_p h_s + 2h_s^2) + E_p^2 h_p^4}{12(E_p h_p + E_s h_s)} \right) l. \tag{22}$$

These expressions are deduced from the theoretical modelling developed in the previous section. It is thus necessary to measure the deflection at the tip of the beam induced by a voltage V in order to compute the value of d_{31}. Two testing benches were set up: one uses the nanoindenter to measure the deflection at the tip of the beam and the other one uses an optical probe. With the optical probe, a DC voltage is simply applied to the film with a controlled amplitude and the deflection is then directly measured at the tip of the beam. The procedure is slightly different with the nanoindenter. The cantilever beam is bent under a controlled and very light force and the resulting deflection is measured. A DC voltage is then applied to the film so that the bending moment created by the voltage forces the deflection of the tip of the beam under the combined load toward its initial position. This is made possible because the indenter is controlled by the initial value of the load. Using these experiments, an average value of the piezoelectric coefficient d_{31} was found:

$$d_{31} = -25 \pm 3 pC/N. \tag{23}$$

Once again, this value is much lower than the value of the bulk, i.e., $-108 pC/N$. The porosity of the films seems to be an explanation for the drop of the electromechanical properties as mentioned previously.

3.3. Mechanical characteristics of our system

The mechanical system is shown in Fig. 1. The alumina and piezoelectric layers have, respectively, the mechanical characteristics given in Table 2 and in Table 3.

Thus, the mechanical characteristics $\bar{\rho}$, A_{11}, B_{11}, D_{11}, $E_{co}I_{co}$ and G_p corresponding to the homogenized coefficients of the beam equations can be computed as shown in Table 4.

There is a difference of about 25% between the homogenized bending stiffness D_{11} and the stiffness derived from static Guyan's condensation $E_{co}I_{co}$ corresponding to the classical Composite Laminated Theory. Thus, the coupling effect between flexural and in-plane motions cannot be avoided by considering only the flexural relationships.

3.4. Experimental set-up for active control tests

The aim of the investigations is to show the capability of this system to induce high damping effect through the control of a piezoceramic layer. For this purpose, the micro-beam is introduced in a feedback loop as described in Fig. 3. The active beam is clamped to a rigid frame of alumina. The piezoelectric plate glued on the frame is used as an external excitator (Fig. 3). A laser vibrometer measures the velocity of the beam at $x = L$ in the mid-width. The output signal of the vibrometer is also amplified and directly applied as a controlling signal on the piezoceramic layer of the beam. As mentioned in the next section, the applied control strategy appears as a quasi-collocated direct-velocity feedback. Indeed, the controlling torque induced by the piezoelectric

Table 2
Mechanical characteristics of the alumina layer

	Value
Length	9.95 mm
Width	2 mm
Thickness	300 μm
Young's modulus	340 GPa
Mass density	3900 kg/m^3
Piezoelectric coefficient (e_{31})	0

Table 2

Table 3
Mechanical characteristics of the piezoelectric layer

	Values
Length	9.95 mm
Width	2 mm
Thickness	110 μm
Young's modulus	22 GPa
Mass density	4000 kg/m^3 (0.5 bulk)
Piezoelectric coefficient (e_{31})	−0.55 N/m V

Table 4
Beam modelling constants

	Values
$\bar{\rho}$	3.22e − 3 kg/m
A_{11}	2.09e + 5 N
B_{11}	−10.49 N m
D_{11}	2.26e − 3 N m^2
$E_{co}I_{co}$	1.73e − 3 N m^2
G_p	−2.20e − 7 N m/V

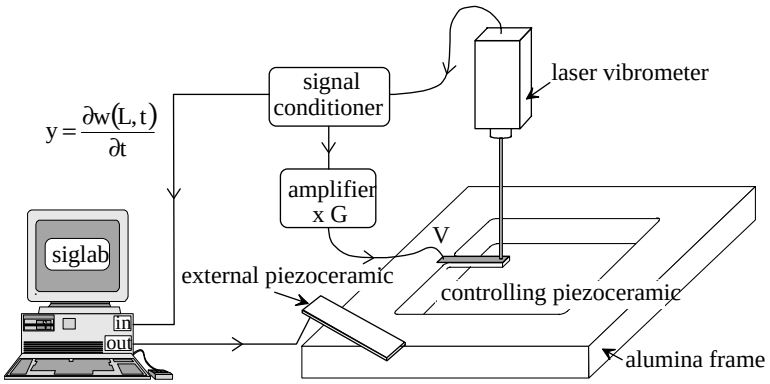

Fig. 3. Experimental set-up: mechanical system and control feedback loop.

layer at the tip of the beam is proportional to the collocated transverse velocity and not to the rotational velocity of the corresponding cross-section. A measurement system Siglab© produces the excitation signal applied to the external piezoelectric plate and measures the output signal of the vibrometer in order to compute the related transfer functions.

3.5. Experimental results

The frequency response functions of the system are computed for different levels of the gain G. Fig. 4 presents two frequency response functions. The dot-line curve represents the response before the control is applied and the solid-line curve corresponds to the maximum value of the gain G.

It can be seen from these curves that the attenuation can reach up to 43 dB. The first eigenmode of the beam is completely damped for this value which means that the critical damping is reached. It is also seen that the second resonance peak at 7.5 kHz is due to a mode involving the alumina frame so that it is not affected by the control. Note that no instability occurred during the test. The maximum gain G is just limited by the power of the voltage amplifier used in the control loop. This experiment seems to show that instability does not appear for this uncollocated system [1].

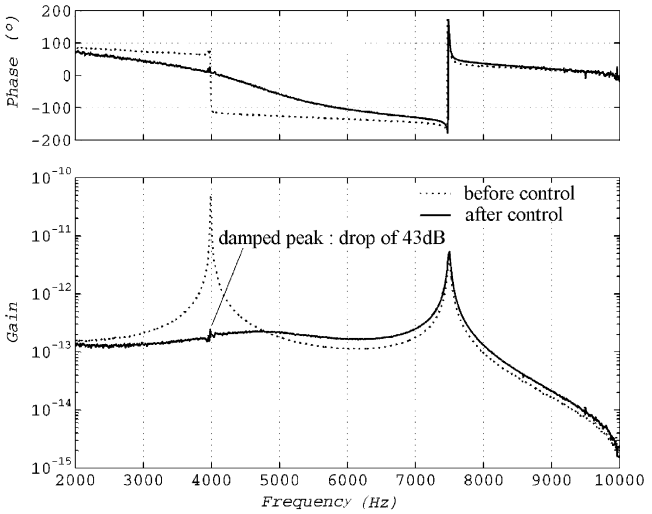

Fig. 4. Frequency response function of a piezocomposite beam before and after control.

4. Theoretical investigations of the pseudo-direct-velocity feedback

The mechanical system modelled in the previous section is controlled according to the strategy presented in Fig. 3. The applied voltage $V(t)$ in Eq. (15) is proportional to the output signal corresponding to the transverse velocity in the form $V(t) = -g\partial w(L,t)/\partial t$. So the boundary control strategy implemented on to the beam appears to be a pseudo-direct-velocity feedback that can be compared with direct-velocity-feedback (DVF) described in Ref. [1]. The applied controlling force and the measured signal are indeed collocated but in this case they do not correspond to dual quantities. A true DVF would lead to a controlling voltage given by $V(t) = -g\partial^2 w(L,t)/\partial t\partial x$ in order to impose dual dissipative term when $g > 0$ as is shown in Ref. [1]. Here the issue is to determine whether this control strategy has the same property of unconditional stability as the collocated DVF or whether it induces instability like an uncollocated system. Note here that the experimental tests have not shown instability.

In order to analyze the evolution of this system as a function of the controlling gain G, two different root locus analysis are presented: the first one is based on a finite element modelling approach and the second one uses the theoretical solutions of the homogenous partial derivative Eqs. (14) and (15) in order demonstrate the unconditional stability of the system.

4.1. Roots locus analysis with finite elements modelling

Apply $V(t) = -g\partial w(L,t)/\partial t$, the partial derivative equations driving the systems (14) and (15) can be rewritten as

$$\bar{\rho}\frac{\partial^2 w(x,t)}{\partial t^2} + E_{co}I_{co}\frac{\partial^4 w(x,t)}{\partial x^4} = 0 \quad \forall x \in]0, L[,$$
$$+ \text{ initial conditions} \tag{24}$$

$$w(0,t) = \frac{\partial w(0,t)}{\partial x} = 0,$$
$$E_{co}I_{co}\frac{\partial^2 w(L,t)}{\partial x^2} = -G\frac{\partial w(L,t)}{\partial t},$$
$$\frac{\partial^3 w(L,t)}{\partial x^3} = 0, \tag{25}$$

where $G = gG_p$. Eqs. (25) have a mixed boundary condition at $x = L$. The variational form of these equations is given in Eqs. (26).

The w solution of Eqs. (24) and (25) is such that

$$\forall \tilde{w} \in L, \quad L = \left\{ \tilde{w} \in H^2(]0,L[), \tilde{w}(0) = \frac{\partial \tilde{w}(0)}{\partial x} = 0 \right\},$$
$$\int_0^L \bar{\rho}\frac{\partial^2 w}{\partial t^2}\tilde{w}\,\mathrm{d}x + G\frac{\partial w(L,t)}{\partial t}\frac{\partial \tilde{w}(L)}{\partial x} + E_{co}I_{co}\int_0^L \frac{\partial^2 w(x,t)}{\partial x^2}\frac{\partial^2 \tilde{w}(x)}{\partial x^2}\,\mathrm{d}x = 0. \tag{26}$$

The beam domain Ω is meshed with n classical two-node isoparametric beam elements [22]. One gets a set of linear differential equations of order $N = 2n$ as described in Eq. (27) with classical mass and stiffness matrices $\mathbf{M}$ and $\mathbf{K}$ elements of $\mathbb{R}^{N\times N}$. The damping matrix $\mathbf{C} \in \mathbb{R}^{N\times N}$ is a dyadic matrix with only one non-zero element located at index $(N-1, N)$ as shown in Eq. (28):

$$\mathbf{M}\ddot{\mathbf{x}} + \mathbf{C}\dot{\mathbf{x}} + \mathbf{K}\mathbf{x} = \mathbf{0}$$
$$+ \text{ initial conditions}, \tag{27}$$

where

$$\mathbf{C} = \mathbf{G}\begin{bmatrix} 0 & \cdots & \cdots & 0 \\ \vdots & \ddots & & \vdots \\ \vdots & & 0 & 1 \\ 0 & \cdots & 0 & 0 \end{bmatrix}. \tag{28}$$

If $\mathbf{C}$ is a semi-definite positive matrix, the linear time-invariant system (27) is stable. It is simple to show that $\mathbf{C}$ is never positive nor negative whatever the value of G is. So it cannot easily be proved that the system modelled according to a classical primal finite element method is stable. A global analysis of the fundamental properties of uncollocated systems can be found in Ref. [1]. The point is also to find out whether the system is unconditionally stable (for any G) or whether there is a maximum G beyond which instability occurs. To study the stability, it is necessary to compute the complex solutions $(\lambda, \mathbf{X}, \mathbf{Y})$ of the quadratic eigenvalue problem (QEP) as in

$$(\lambda^2\mathbf{M} + \lambda\mathbf{C} + \mathbf{K})\mathbf{X} = \mathbf{0}, \quad \mathbf{Y}^*(\lambda^2\mathbf{M} + \lambda\mathbf{C} + \mathbf{K}) = \mathbf{0}. \tag{29}$$

Here $\mathbf{Y}$ is the left eigen values matrix, $\mathbf{X}$ the right one. It is known that if the complex eigenvalue λ has a negative real part, the corresponding mechanical system is stable. Unfortunately, the system governed by Eq. (27) is never Hermitian nor skew-Hamiltonian so a dedicated numerical procedure must be used. In the next section, the computation was done using the Matlab polyeig $(\mathbf{K}, \mathbf{C}, \mathbf{M})$ direct method which is able to solve this unsymmetric QEP as described in Ref. [23].

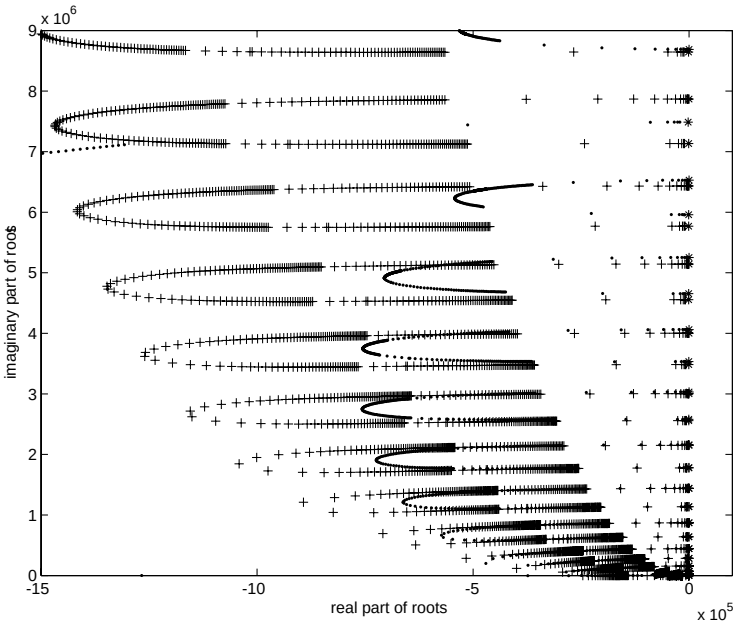

Fig. 5. Root locus of the mechanical system modelling with finite elements: + 20 elements; ·10 elements. $G = 1 \cdot e{-}5 \rightarrow 1$.

Fig. 5 shows the root locus of the system modelling by Eq. (27) as a parametric function of G. In this figure, the values of G are in the range $1 \cdot e{-}5$ to 1. The same locus is computed using 10 finite elements (shown by ·) and 20 (shown by +). No unstable root appears even for high frequencies corresponding to "numerical modes".

Note in Fig. 5 that the high-frequency roots never reach the critical damping (these roots do not become real). Considering the zoom of the root locus for the first three modes (Fig. 6), the first two modes become critical for high controlling gain G. However, when the mesh density increases the high-frequency root loops grow. Note the very high sensitivity of the results to the mesh density; it appears to be numerically difficult to reach the asymptotic behavior of the system.

The starting roots correspond of course to the undamped real eigenfrequencies of the cantilever beam, which are close to the experimental values. When $G \rightarrow +\infty$, the first ending roots reach 0 and then infinity, which means that it remains critical for G to exceed a threshold value G_c. As far as they are concerned, the other complex eigenfrequencies converge towards the eigenfrequencies of the bi-pinned beam when $G \rightarrow +\infty$!

Table 5 shows the numerical real eigenfrequencies for $G = 0$ and when $G \rightarrow +\infty$. We also indicate the values of the theoretical and measured eigenfrequencies of the corresponding cantilever and bi-pinned beam in Table 6.

The eigenshapes corresponding to the first four modes are shown in Fig. 7 for $G = 0$ and in Fig. 8 when $G \rightarrow +\infty$.

Fig. 7 shows the classical first four modes of a cantilever beam but in Fig. 8, the shapes of modes 2–4 appear to be those of a clamped–pinned beam. The first one corresponding to an eigenvalue of 0 Hz remains the same as the first mode of the uncontrolled cantilever beam.

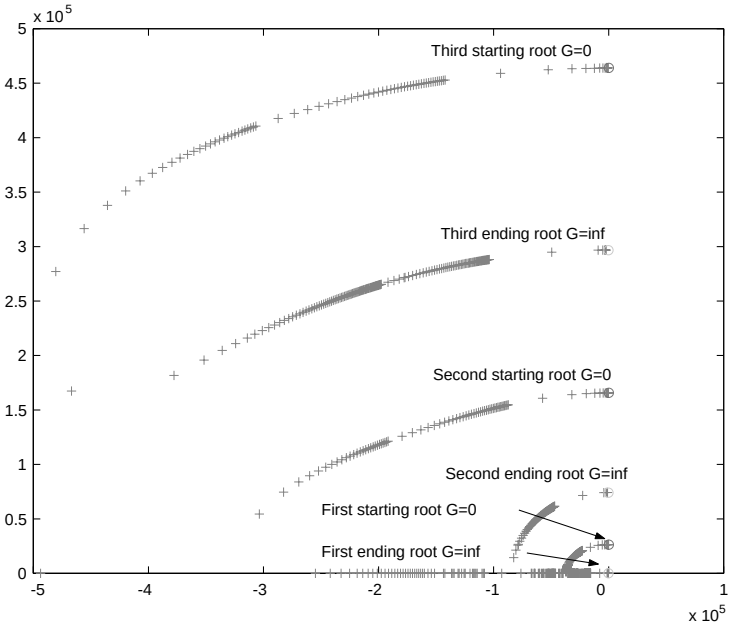

Fig. 6. Root locus of the first three complex eigenfrequencies for the system modelling with finite elements.

Table 5
Eigenfrequencies (in Hz) computed with finite elements approach

Modes	Computed starting roots	Computed ending roots
1	4028	0
2	2.52e + 4	1.12e + 4
3	7.07e + 4	4.57e + 4
4	1.38e + 5	1.01e + 5
5	2.29e + 5	1.86e + 5

Table 5
Eigenfrequencies (in Hz) computed with finite elements approach

Table 6
Theoretical and experimental eigenfrequencies (in Hz)

Modes	Theoretical modes of the cantilever beam	Theoretical modes of the bi-pinned beam	Experimental modes at $G = 0$	Experimental modes at $G \to \infty$
1	4028	/	4020	0
2	2.52e + 4	1.13e + 4	2.55e + 4	Not measured
3	7.07e + 4	4.52e + 4	Not measured	Not measured
4	1.38e + 5	1.02e + 5	Not measured	Not measured
5	2.29e + 5	1.81e + 5	Not measured	Not measured

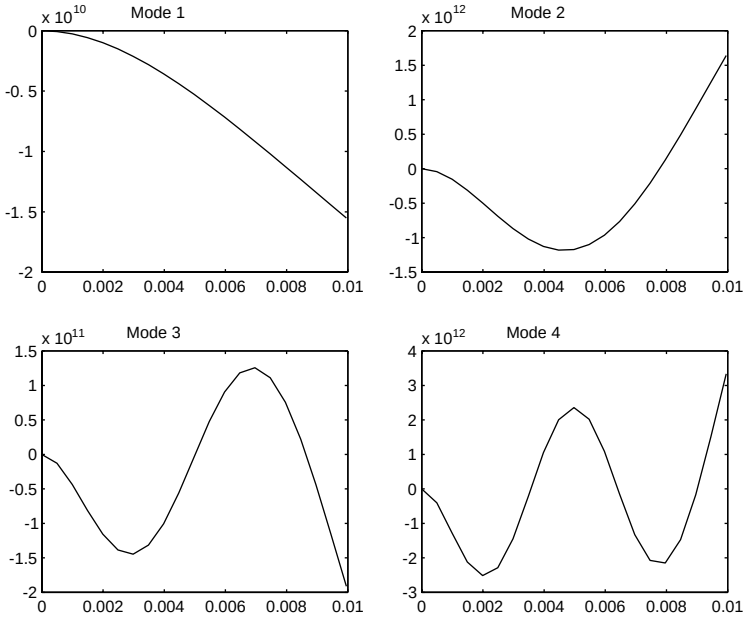

Fig. 7. The first four mode shapes of the system when $G = 0$.

Concluding remarks on this first part of the study are as follows:

- the modelling using a finite element approach lead to a sensitive meshing finite system.
- the first two modes become critical for any values of the gain G; the corresponding first root remains real negative while the second tends to the imaginary root of the first bi-pinned mode of the same beam when $G \to +\infty$.
- the other modes remain complex and tend towards the modes of the bi-pinned beam when $G \to +\infty$.
- the mode shapes corresponding to the asymptotic bi-pinned eigenfrequencies are those of a clamped–pinned beam.

These surprising results need to be confirmed through another theoretical approach to discarded the finite elements functional assumptions which can induce errors for boundary control strategies [14,15] and the numerical errors due to the complex eigenvalues computation with a Jordan damping matrix C.

4.2. Theoretical locus analysis of the partial derivative equations roots

4.2.1. Characteristic equation of the controlled system

The homogeneous partial derivative Eqs. (24) and (25) describe the motion of the mechanical system (Fig. 3) when the control strategy imposes $V(t) = -g\partial w(L,t)/\partial t$. Assume the field of displacement $w(x,t)$ to be written as

$$w(x,t) = f(t)h(x). \tag{30}$$

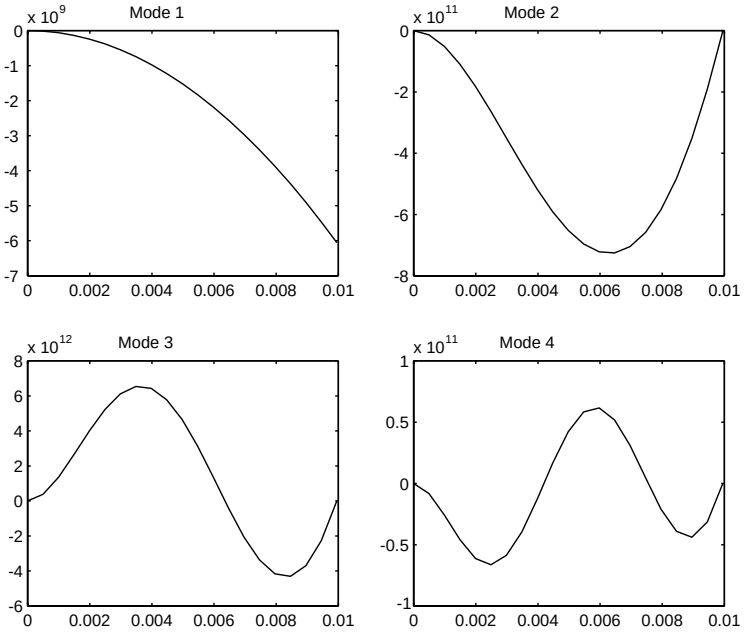

Fig. 8. The first four mode shapes of the system when $G \to +\infty$.

The motion equation can be rewritten as

$$\bar{\rho}h(x)\frac{\mathrm{d}^2 f(t)}{\mathrm{d}t^2} + E_{co}I_{co}\frac{\mathrm{d}^4 h(t)}{\mathrm{d}x^4}f(t) = 0 \\ + \text{ initial conditions.} \tag{31}$$

Eq. (32) expresses the classical form of the complex solution of the homogeneous differential Eq. (31):

$$\exists s, f_o \in \mathbb{C}^2 / f(t) = f_o \mathrm{e}^{st}, \\ \exists (a,b,c,d) \in \mathbb{C}^4 h(x) = a\mathrm{e}^{kx} + b\mathrm{e}^{-kx} + c\mathrm{e}^{\mathrm{i}kx} + d\mathrm{e}^{-\mathrm{i}kx}, \tag{32}$$

where $\mathrm{i}^2 = -1$ and

$$k^4 = -\frac{\bar{\rho}s^2}{E_{co}I_{co}}. \tag{33}$$

f_o is computed from the initial conditions. (a,b,c,d) and k are calculated with the boundary conditions given in Eqs. (25). These conditions lead to

$$a + b + c + d = 0, \\ ka - kb + \mathrm{i}kc - \mathrm{i}kd = 0,$$

$$k^3(a\mathrm{e}^{kL} - b\mathrm{e}^{-kL} - \mathrm{i}c\mathrm{e}^{\mathrm{i}kL} + \mathrm{i}d\mathrm{e}^{-\mathrm{i}kL}) = 0,$$
$$k^2(a\mathrm{e}^{kL} + b\mathrm{e}^{-kL} - c\mathrm{e}^{\mathrm{i}kl} - d\mathrm{e}^{-\mathrm{i}kL}) = -\frac{G}{E_{co}I_{co}}s(a\mathrm{e}^{kL} + b\mathrm{e}^{-kL} + c\mathrm{e}^{\mathrm{i}kL} + d\mathrm{e}^{-\mathrm{i}kL}). \quad (34)$$

The last equation of (34) can be simplified using Eq. (33) and assuming first that $s = +\mathrm{i}\sqrt{E_{co}I_{co}/\bar{\rho}}k^2$:

$$\begin{bmatrix} 1 & 1 & 1 & 1 \\ 1 & -1 & i & -i \\ \mathrm{e}^{kL} & -\mathrm{e}^{-kL} & -\mathrm{i}\mathrm{e}^{\mathrm{i}kL} & \mathrm{i}\mathrm{e}^{-\mathrm{i}kL} \\ \mathrm{e}^{kL}(1-\mathrm{i}\lambda) & \mathrm{e}^{-kL}(1-\mathrm{i}\lambda) & \mathrm{e}^{\mathrm{i}kL}(1+\mathrm{i}\lambda) & \mathrm{e}^{-\mathrm{i}kL}(1+\mathrm{i}\lambda) \end{bmatrix} \begin{bmatrix} a \\ b \\ c \\ d \end{bmatrix} = 0, \quad (35)$$

where $\lambda = \sqrt{\bar{\rho}E_{co}I_{co}}/G$. Eq. (35) as a non-trivial solution if and only if

$$\left| \begin{bmatrix} 1 & 1 & 1 & 1 \\ 1 & -1 & i & -i \\ \mathrm{e}^{kL} & -\mathrm{e}^{-kL} & -\mathrm{i}\mathrm{e}^{\mathrm{i}kL} & \mathrm{i}\mathrm{e}^{-\mathrm{i}kL} \\ \mathrm{e}^{kL}(1-\mathrm{i}\lambda) & \mathrm{e}^{-kL}(1-\mathrm{i}\lambda) & \mathrm{e}^{\mathrm{i}kL}(1+\mathrm{i}\lambda) & \mathrm{e}^{-\mathrm{i}kL}(1+\mathrm{i}\lambda) \end{bmatrix} \right| = 0. \quad (36)$$

The new variables α and β can be introduced so that $kL = \alpha + \mathrm{i}\beta$, so that the complex characteristic Eq. (36) can be rewritten according to its real and imaginary parts, respectively, as follows:

$$\sinh(\alpha - \beta)\sin(\alpha + \beta)(\lambda + 1) - \sinh(\alpha + \beta)\sin(\alpha - \beta)(\lambda - 1) = 0, \quad (37)$$

$$2\lambda + \cos(\alpha + \beta)\cosh(\alpha - \beta)(\lambda + 1) + \cos(\alpha - \beta)\cosh(\alpha + \beta)(\lambda - 1) = 0. \quad (38)$$

Since $s = +\mathrm{i}\sqrt{E_{co}I_{co}/\bar{\rho}}k^2$, the complex pulsation is given as

$$s = \sqrt{\frac{E_{co}I_{co}}{\bar{\rho}L^4}}(-2\alpha\beta + \mathrm{i}(\alpha^2 - \beta^2)). \quad (39)$$

If $\bar{s} = -\mathrm{i}\sqrt{E_{co}I_{co}/\bar{\rho}}k^2$ is introduced into Eq. (34), the parameter λ becomes $-\lambda$ in Eqs. (36)–(38). Writing $kL = \alpha - \mathrm{i}\bar{\beta}$ instead of $\alpha + \mathrm{i}\beta$, the system is of course the same and the final pulsation is $\bar{s} = \sqrt{E_{co}I_{co}/\bar{\rho}L^4}(2\alpha\bar{\beta} + \mathrm{i}(\alpha^2 - \bar{\beta}^2)) = s$ because $\bar{\beta} = -\beta$. Thus, the choice of the expression of s in Eq. (34) does not change the final result in Eq. (39).

4.2.2. Analysis of the solutions of the characteristic equations

It is assumed that some solutions exist of the non-linear transcendental system (37) and (38). The constructive proof of this result is presented in the next section with the numerical estimation of these solutions. By considering Eqs. (37) and (38), the asymptotic eigenvalues of the system when $G = 0$ and $G \to +\infty$ can be determined

- $G = 0$, $\lambda \to +\infty$

Eqs. (37) and (38) are rewritten in Eqs. (40) and (41):

$$\sinh(\alpha-\beta)\sin(\alpha+\beta)-\sinh(\alpha+\beta)\sin(\alpha-\beta)=0, \tag{40}$$

$$2+\cos(\alpha+\beta)\cosh(\alpha-\beta)+\cos(\alpha-\beta)\cosh(\alpha+\beta)=0. \tag{41}$$

As the uncontrolled system is undamped, it is easy to show that the solutions of Eqs. (40) and (41) are obtained for $\alpha=0$ or $\beta=0$. So, assuming $\beta=0$, the eigenvalues α_i are the solutions of the transcendental characteristic equation (42) which is the characteristic equation of the cantilever beam [24]. According to Eq. (39), the same eigenvalues s_i for $\alpha=0$ are obtained.

$$1+\cos(\alpha_i)\cosh(\alpha_i)=0. \tag{42}$$

- $G\to+\infty$, $\lambda=0$

Eqs. (37) and (38) are rewritten, respectively, as follows:

$$\sinh(\alpha-\beta)\sin(\alpha+\beta)+\sinh(\alpha+\beta)\sin(\alpha-\beta)=0, \tag{43}$$

$$\cos(\alpha+\beta)\cosh(\alpha-\beta)-\cos(\alpha-\beta)\cosh(\alpha+\beta)=0. \tag{44}$$

If two variables $x=\alpha+\beta$ and $y=\alpha-\beta$ are introduced, Eqs. (43) and (44) become

$$sh(y)\sin(x)+sh(x)\sin(y)=0, \tag{45}$$

$$\cos(x)ch(y)-\cos(y)ch(x)=0. \tag{46}$$

If $(x,y)\in\mathbb{R}^2$ is a solution of the system (45) and (46), it is also a solution of the following system

$$\cos(x-\mathrm{i}y)=\cos(x-\mathrm{i}y), \tag{47}$$

$$\cos(x+\mathrm{i}y)=\cos(x+\mathrm{i}y). \tag{48}$$

The product of Eqs. (47) and (48) leads to the equation

$$\cos(2x)-\cosh(2x)=\cos(2y)-\cosh(2y). \tag{49}$$

$t(X)=\cos(X)-\cosh(X)$ is a decreasing symmetric function under $\mathbb{R}$. So (x,y) solution of Eq. (49) implies that $x=y$ ($\beta=0$) or $x=-y$ ($\alpha=0$). The calculated eigenfrequencies are also purely imaginary ($\alpha=0$ or $\beta=0$).

If $\beta=0$ is first considered, the eigenvalues α_i are given by the equation

$$\sinh(\alpha_i)\sin(\alpha_i)=0. \tag{50}$$

Also $\alpha_i=j\pi$ for $j\in\mathbb{N}$. The eigenfrequencies of the corresponding bi-pinned beam and 0 are obtained. These results confirm those obtained in the previous section by using a finite elements modelling.

If now, it is assumed that $\alpha=0$, exactly the same results for β are obtained.

The asymptotic behavior of the roots characterizing the homogeneous differential system (24), (25) have been described. The same properties as those for the finite elements approach have been found. The next question is: is the system stable for any value of the gain G?

The following theorem can be proved.

Theorem 1. $\forall G \in [0, +\infty[$ *the solutions of Eqs.* (37) *and* (38) *satisfy* $\alpha\beta \geqslant 0$.

Proof. If $x = \alpha + \beta$, $y = \alpha - \beta$ $\forall G \in [0, +\infty[$, $\lambda \in [0, +\infty[$. Eqs. (37) and (38) can be rewritten as

$$f(x, y, \lambda) = (1 + \lambda)\sinh(y)\sin(x) + (1 - \lambda)\sinh(x)\sin(y) = 0, \tag{51}$$

$$g(x, y, \lambda) = 2\lambda + (1 + \lambda)\cos(x)\cosh(y) - (1 - \lambda)\cos(y)\cosh(x) = 0. \tag{52}$$

The eigenfrequency given by Eq. (39) is then written as $s(x, y, \lambda) = \sqrt{E_{co}I_{co}/\bar{\rho}L^4}(-(x^2 - y^2)/2 + \mathrm{i}xy)$ where (x, y, λ) verify Eqs. (51) and (52). $s(x, y, \lambda) \in C^o(\mathbb{R} \times \mathbb{R} \times \mathbb{R}^+ \to \mathbb{C})$. It is symmetric with respect to x and y so that the analysis is restricted to $\mathbb{R}^+ \times \mathbb{R}^+ \times \mathbb{R}^+$.

If $\mathrm{Re}(s(x, y, \lambda)) = 0$ then $x = y$ or $x = -y$. Eqs. (51) and (52) become

$$\begin{aligned} &\frac{2}{1 + \lambda}\sinh(x)\sin(x) = 0, \\ &\frac{2\lambda}{1 + \lambda} + \frac{2\lambda}{1 + \lambda}\cos(x)\cosh(x) = 0. \end{aligned} \tag{53}$$

The first equation is satisfied if $\lambda = +\infty$ or if $\exists j \in \mathbb{N}$ so that $x = j\pi$.

If $\lambda = +\infty$, the second equation is $1 + \cos(x)ch(x) = 0$ which of course corresponds to Eq. (42).

If $\exists j \in \mathbb{N}$ so that $x = j\pi$, the second equations become $2\lambda/(1 + \lambda) + (2\lambda/(1 + \lambda))(-1)^j \cosh(j\pi) = 0$ which is absurd for any value of j if $\lambda \neq 0$. So the unique solution is obtained for $\lambda = 0$ and the corresponding eigenvalues are those given by Eq. (50).

Finally, the unique purely imaginary solutions are obtained for $\lambda = 0$ (corresponding to the bi-pinned beam) or $\lambda = +\infty$ (corresponding to the cantilever beam). By using the continuity property of $s(x, y, \lambda)$, it can be shown that any solution is complex with a negative real part only by analyzing the roots location around one of these asymptotic values. (For example, consider the location of (x, y, λ) around $(j\pi, j\pi, 0)$, the ending eigenvalues computed with $\lambda = 0$ $(G = +\infty)$.) By using Eqs. (51) and (52),

$$\begin{aligned} \frac{\partial g}{\partial x}(j\pi, j\pi, 0) &= (-1)^{j+1}\sinh(j\pi), \\ \frac{\partial g}{\partial y}(j\pi, j\pi, 0) &= (-1)^j \sinh(j\pi), \end{aligned} \tag{54}$$

$$\frac{\partial g}{\partial \lambda}(j\pi, j\pi, 0) = 2((-1)^j \cosh(j\pi) + 1). \tag{55}$$

So along the trajectory of any roots around the starting point at $\lambda = 0$:

$$\begin{aligned} \frac{\partial x}{\partial \lambda}(j\pi, j\pi, 0) &= 2\frac{(-1)^j \cosh(j\pi) + 1}{(-1)^j \sinh(j\pi)} > 0 \quad \forall j \in \mathbb{N}, \\ \frac{\partial y}{\partial \lambda}(j\pi, j\pi, 0) &= -2\frac{(-1)^j \cosh(j\pi) + 1}{(-1)^j \sinh(j\pi)} < 0 \quad \forall j \in \mathbb{N}. \quad \square \end{aligned} \tag{56}$$

So when λ increases, x decreases and y increases which induces $x > y$ then real$(s(x, y, \lambda)) < 0$ for (x, y, λ) around $(j\pi, j\pi, 0)$ in $\mathbb{R}^+ \times \mathbb{R}^+ \times \mathbb{R}^+$. By continuity, this result proves that $\forall G \in [0, +\infty[$, the solutions of Eqs. (37) and (38) verify $\alpha\beta \geqslant 0$.

This theorem implies that all the solutions of Eqs. (37) and (38) are *stable* for any value of G. This result proves the previous observation made on the basis of a finite elements approach.

4.2.3. Theoretical roots locus computation and analysis

The complex roots of the initial controlled system (14), (15) are given by solving the set of transcendental Eqs. (37) and (38). Fig. 9 shows the parametric curves corresponding to each equation to be solved for $G = 1 \cdot e - 2$. The intersection points are the complex solutions of the system. It is immediately shown that all roots presented in Fig. 9 are stable as previously demonstrated.

Fig. 10 represents the root locus solution of Eqs. (37) and (15) as a parametric function of G. As previously mentioned, the unstable root does not occur whatever the gain G is. A second property shown in Fig. 5 indicates that the high-frequency roots reach the critical damping (these roots become real for very high values of G). This result does not correspond to those given by the computation based on finite element modelling but represents the asymptotic behavior of this system.

A closer look at a zoom of the root locus of the first three modes (Fig. 11), shows that all these modes become critical for high controlling gain G. The starting roots of course correspond to the undamped real eigenfrequencies of the cantilever beam. When G tends to infinity, the first ending roots reach 0 and infinity. The other modes become critical for some values of G but tend towards the purely imaginary eigensolutions of the bi-pinned beam when G tends towards infinity. It is a specific property of this system.

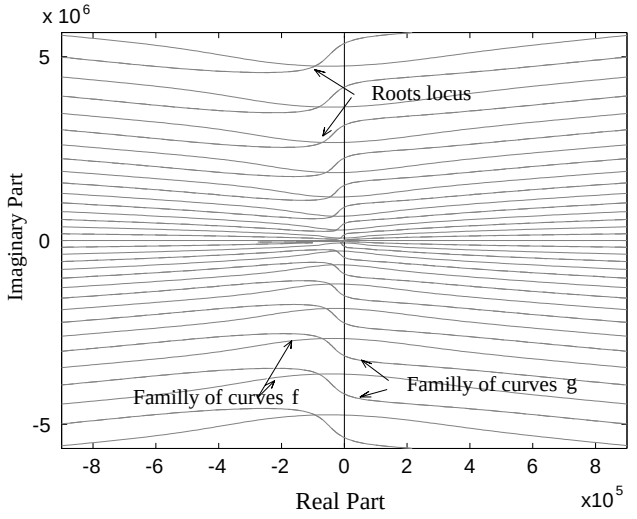

Fig. 9. f, g curves families and roots locus corresponding to the intersection points. $G = 1 \times 10^{-2}$.

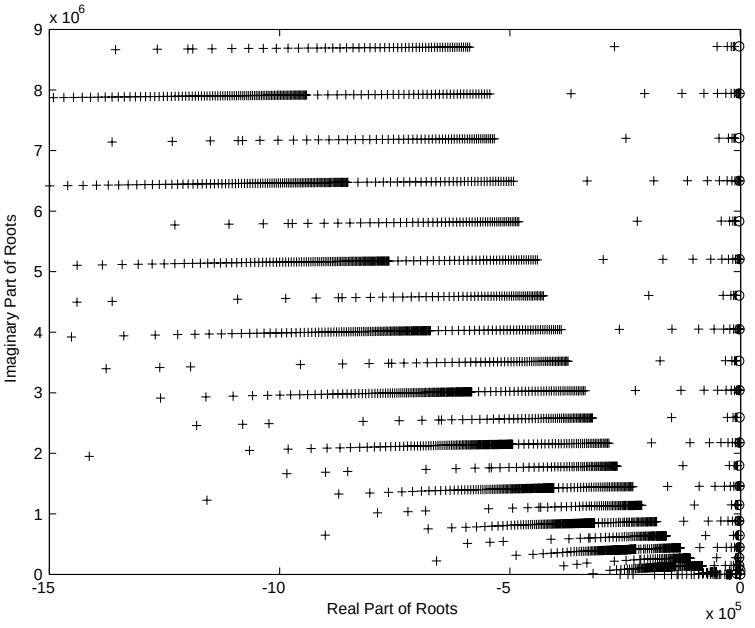

Fig. 10. Theoretical roots locus ($s(G)$) in the complex plane. $G = 1.e-5 \rightarrow 1$.

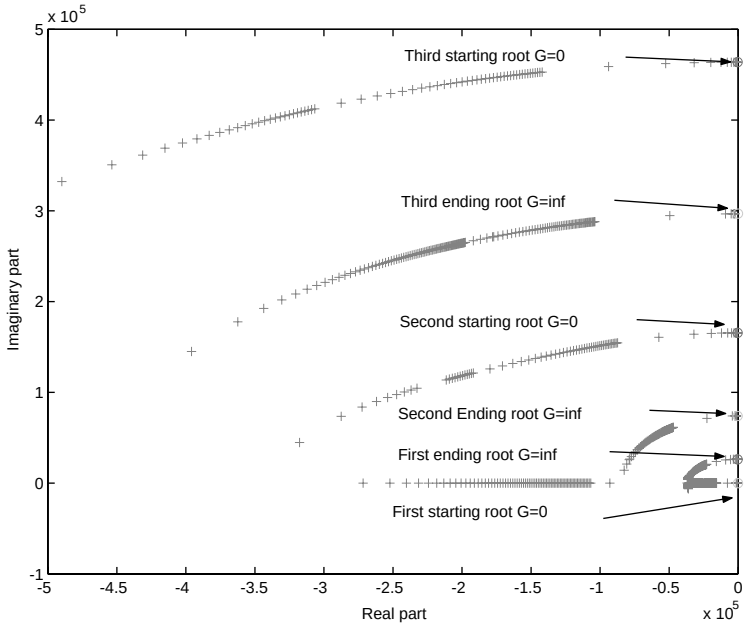

Fig. 11. First three theoretical roots locus in the complex plane.

Table 7 shows the numerical real eigenfrequencies for $G = 0$ and $G \rightarrow +\infty$. The values of the theoretical eigenfrequencies of the corresponding cantilever and bi-pinned beam are indicated in Table 6. These results correspond to those obtained with the finite elements approach.

Table 7
Eigenfrequencies (in Hz) computed with the direct method

Modes	Computed starting roots	Computed ending roots
1	4084	0
2	2.56e + 4	1.14e + 4
3	7.17e + 4	4.58e + 4
4	1.40e + 5	1.03e + 5
5	2.32e + 5	1.83e + 5

Table 7
Eigenfrequencies (in Hz) computed with the direct method

As a concluding remark on this third part of the study, the following points are made:

- the theoretical approach demonstrates that the system studied is always stable whatever the value of the controlling gain G is.
- all the modes become critical when the gain G increases. When $G \to +\infty$, the first root is still real negative while the others tend towards the purely imaginary root of the bi-pinned mode of the same beam.
- the results of this analysis are not exactly the same as those derived from the finite element approach. The difficulty of working with the classical mechanical modelling strategies when studying the behavior of a controlled structure is noted; particularly when the residual behavior appears important when describing the controlled system. Other authors [11,14,15] have made the same points for other systems.

5. Concluding remarks

The experiment presented in this paper shows the real efficiency of the hard-PZT thick films in actuating micro-structures. It is observed that the typical attenuation can reach up to 43 dB on the first mode before being critical without inducing spill-over instability. While this structure is not strictly collocated, this result appears very surprising [1,12]. Thus, the classical property of conditional unstability of the non-collocated controlled systems may be refuted.

Secondly, it is shown that the real mechanical behavior of the controlled system is difficult to model by using the classical finite element method. Indeed the finite system tends slowly to the continuous one because of the residual terms which greatly affect the controlled behavior for some values of G. Nevertheless, the computed roots for $G = 0$ and $G \to +\infty$ are predicted well. The roots also tend towards the eigenfrequencies of the bi-pinned beam when the controlling gain $G \to +\infty$ while the corresponding eigenshapes correspond to the shapes of a clamped–pinned beam with the same geometry.

The theoretical approach demonstrates that all roots of the controlled structure are always stable whatever the controlling gain G is. In fact, it demonstrates that the gramian given by the following equation is coercive when w is solution of Eqs. (24) and (25):

$$J(w, w) = \frac{\partial w(L, t)}{\partial t} \frac{\partial^2 w(L, t)}{\partial x \partial t}. \tag{57}$$

These results underline the necessity to use some specific techniques to study the controlled behavior of a continuous structure as reported by [10,11,14,15]. Applying directly automation tools on finite element modelling of the mechanical system can lead to numerical misunderstanding, as described in this paper. As more and more efficient actuators are used in the systems, it appears essential to develop new numerical tools dedicated to the design of a structural boundary control strategy, especially for MicroElectroMechanicalSystem applications.

References

[1] A. Preumont, Vibration Control of Active Structures, An Introduction, Kluwer, Dordrecht, 1997.
[2] H.T. Banks, R.C. Smith, Y. Wang, Smart Material Structures: Modeling, Estimation and Control, Wiley, Chichester and Masson, Paris, 1996.
[3] C.K. Lee, Laminated piezopolymer plates for torsion and bending sensors and actuators, Journal of the Acoustical Society of America 85 (6) (1989) 2432–2439. doi: 10.1121/1.397792.
[4] C.K. Lee, Theory of laminated piezoelectric plates for design of distributed sensors/actuators, part I: governing equations and reciprocal relationships, Journal of the Acoustical Society of America 87 (3) (1990) 1144–1158. doi: 10.1121/1.398788.
[5] C.K. Lee, W.-W. Chiang, T.C. O'Sullivan, Piezoelectric modal sensor/actuator pairs for critical active damping vibration control, Journal of the Acoustical Society of America 90 (1) (1991) 374–384. doi: 10.1121/1.401260.
[6] U. Lee, J. Kim, Spectral element modelling for the beams treated with active constrained layer damping, International Journal of Solids and Structures 38 (2001) 5679–5702. doi: 10.1016/s0020-7683(00)00360-7.
[7] H.S. Tzou, H.Q. Fu, A study of segmentation of distributed piezoelectric sensors and actuators, part I: theoretical analysis, Journal of Sound and Vibration 172 (2) (1994) 247–259. doi: 10.1006/jsvi.1994.1172.
[8] H.S. Tzou, H.Q. Fu, A study of segmentation of distributed piezoelectric sensors and actuators, part II: parametric study and active vibration controls, Journal of Sound and Vibration 172 (2) (1994) 261–275. doi: 10.1006/jsvi.1994.1173.
[9] P. Gaudenzi, R. Carbonaro, E. Benzi, Control of beam vibrations by means of piezoelectric devices: theory and experiments, Journal of Composite Structures 50 (2000) 376–379.
[10] A. Lara, J.C. Bruch Jr., Vibration damping in beams via piezo actuation using optimal boundary control, International Journal of Solids and Structures 337 (2000) 6537–6554.
[11] J.M. Sloss, J.C. Bruch Jr., Piezoelectric patch control using an integral equation approach, Thin-Walled Structures 39 (2001) 45–63. doi: 10.1016/s0263-8231(00)00053-7.
[12] M. Collet, Active control with piezoelectric layers optimization, Journal of Structural Control 1 (1995) 59–79.
[13] A. Hac, L. Liu, Sensor and actuator location in motion control of flexible structures, Journal of Sound and Vibration 167 (2) (1993) 239–261. doi: 10.1006/jsvi.1993.1333.
[14] F. Bourquin, M. Collet, Some modelling and numerical issue for the control of flexible structure and their practical impact, in: Proceedings of the 13rd International Workshop on Structural Control, LCPC, Paris, 2000.
[15] F. Bourquin, M. Collet, J.F. Briffaud, On the feedback stabilization: Komornik's methods, in: T. Kobori, Y. Inoue, K. Seto, H. Iemura, A. Nishitani (Eds.), Proceedings of the Second International Conference on Active Control in Mechanical Engineering 1987–1997, Wiley, New York, 1997.
[16] M.O.M. Carvalho, M. Zindeluk, Active control of waves in a Timoshenko beam, International Journal of Solids and Structures 38 (2001) 1749–1764.
[17] Y. Yee, H.J. Nam, PZT actuated micromirror for fine-tracking mechanism of high-density optical data storage, Sensors and Actuators: A Physical 89 (2001) 166–173. doi: 10.1016/s0924-4247(00)00535-5.
[18] L. Seffner, H.J. Gesemann, Preparation and application of PZT thick films, in: Proceedings of the Fourth International Conference on Electrical Ceramics and Applications, Electroceramics IV, Vol. 1, 1994, pp. 317–320.
[19] A. Tylikowski, Effects of piezoactuator delamination on the transfer functions of vibration control systems, International Journal of Solids and Structures 38 (2001) 2189–2202. doi: 10.1016/s0020-7683(00)00161-x.

[20] V. Tajan, P. Gonnard, M. Troccaz, Elaboration of PZT thick films by screen-printing, in: P.-F.P. Gobin (Ed.), 3rd International Conference on Intelligent Materials and 3rd European Conference on Smart Structures and Materials, SPIE Proceedings, Vol. 2779, SPIE, Bellingham, WA, 1996, pp. 564–569.
[21] W.C. Oliver, G.M. Pharr, An improved technique for determining hardness and elastic modulus using load and displacement sensing indentation experiments, Journal of Materials Research 7 (6) (1992) 1564–1583.
[22] K. Bathe, Finite Element Procedures in Engineering Analysis, Prentice-Hall, Englewood Cliffs, NJ, 1982.
[23] F. Tisseur, K. Meerbergen, The quadratic eigenvalue problem, SIAM Review 43 (2) (2001) 235–286.
[24] M. Geradin, Mechanical Vibrations. Theory and Application to Structural Dynamics, Wiley, Chichester and Masson, Paris, 1994.